


## Article

# Simultaneously Cationic and Anionic Dyes Elimination via Magnetic Hydrochar Prepared from Copper Slag and Pinewood Sawdust

Huabin Wang <sup>1,\*</sup> , Yi Wu <sup>1</sup>, Yi Wen <sup>1</sup>, Dingxiang Chen <sup>1</sup>, Jiang Pu <sup>2</sup>, Yu Ding <sup>3</sup>, Sailian Kong <sup>4</sup>, Shuaibing Wang <sup>5</sup> and Rui Xu <sup>1,\*</sup>

<sup>1</sup> School of Energy and Environment Science, Yunnan Normal University, Kunming 650500, China; wuyimax@foxmail.com (Y.W.); wyaquarius@foxmail.com (Y.W.); ynnuchendx@foxmail.com (D.C.)

<sup>2</sup> Shipping Center for Rural Energy and Environment, Honghe 661400, China; 13867455685@163.com

<sup>3</sup> Baoshan City Longyang Rural Energy Workstation, Baoshan 678000, China

<sup>4</sup> Development Center for Rural Affairs of Jiangchuan District, Yuxi 651100, China; yunnanxt@foxmail.com

<sup>5</sup> College of Chemistry Biology and Environment, Yuxi Normal University, Yuxi 653100, China; wshuaibing@yxnu.edu.cn

\* Correspondence: hbwang@ynnu.edu.cn (H.W.); ecowatch\_xr@163.com (R.X.); Tel./Fax: +86-27-87792151 (R.X.)

**Abstract:** In practical wastewater, cationic and anionic dyes usually coexist, while synergistic removal of these pollutants is difficult due to their relatively opposite properties. In this work, copper slag (CS) modified hydrochar (CSHC) was designed as functional material by the one-pot method. Based on characterizations, the Fe species in CS can be converted to zero-valent iron and loaded onto a hydrochar substrate. The CSHC exhibited efficient removal rates for both cationic dyes (methylene blue, MB) and anionic dyes (methyl orange, MO), with a maximum capacity of 278.21 and 357.02 mg·g<sup>-1</sup>, respectively, which was significantly higher than that of unmodified ones. The surface interactions of MB and MO between CSHC were mimicked by the Langmuir model and the pseudo-second-order model. In addition, the magnetic properties of CSHC were also observed, and the good magnetic properties enabled the adsorbent to be quickly separated from the solution with the help of magnets. The adsorption mechanisms include pore filling, complexation, precipitation, and electrostatic attraction. Moreover, the recycling experiments demonstrated the potential regenerative performance of CSHC. All these results shed light on the co-removal of cationic and anionic contaminants via these industrial by-products derived from environmental remediation materials.

**Keywords:** modified hydrochar; copper slag; dyes; simultaneous removal; adsorption mechanisms



**Citation:** Wang, H.; Wu, Y.; Wen, Y.; Chen, D.; Pu, J.; Ding, Y.; Kong, S.; Wang, S.; Xu, R. Simultaneously Cationic and Anionic Dyes Elimination via Magnetic Hydrochar Prepared from Copper Slag and Pinewood Sawdust. *Toxics* **2023**, *11*, 484. <https://doi.org/10.3390/toxics11060484>

Academic Editors: Junhao Qin, Peidong Su, Feng Zhu and Lin Ding

Received: 11 April 2023

Revised: 21 May 2023

Accepted: 23 May 2023

Published: 25 May 2023



**Copyright:** © 2023 by the authors. Licensee MDPI, Basel, Switzerland. This article is an open access article distributed under the terms and conditions of the Creative Commons Attribution (CC BY) license (<https://creativecommons.org/licenses/by/4.0/>).

## 1. Introduction

With the rapid development of social industry and textile scale, the immature technology of dye wastewater treatment systems leads to a large number of compounds and intermediates participating in the process of dye production and dyeing. As the wastewater is discharged into external water bodies, the treatment capacity of dye wastewater also decreases [1,2]. The ecological and environmental problems caused by printing and dyeing wastewater are inevitable and ubiquitous in daily life [3]. The printing and dyeing wastewater is a typical high-pollution wastewater, which is characterized by large discharge, high chroma, high salt concentration, strong acid, strong alkali, strong resistance to microorganisms, and so on [4,5]. Some organic compounds and toxic heavy metals pose carcinogenic, teratogenic, and mutagenic risks to humans [6]. In addition, due to the variety of dyes and complex industrial production, there are always different kinds of dye residues in the wastewater, that is, anionic dyes and cationic dyes always coexist [7]. However, the physical and chemical properties of anionic and cationic dyes are basically opposite, and it is usually difficult to remove both dyes at the same time.

Coagulation and flocculation, precipitation, microbial, electrolysis, adsorption, and membrane separation are currently commonly used to remove dyes [8,9]. However, each method has its advantages and disadvantages. For example, although the microbial method can utilize cheap renewable resources, the microbial growth and culture path is long, so it is easy to produce more by-products in the follow-up experiment, and the reaction cycle is long. The membrane separation method is simple to operate and has little pollution, but with the increase of the use time, the surface of the membrane will be polluted, which reduces the performance. Moreover, this method only separates and transfers the pollutants and cannot fundamentally achieve adsorption. According to previous studies, the adsorption method still has advantages, which are far ahead of other methods in terms of application value and actual removal effect. At the same time, it has the advantages of good removal effect, short time, low cost, simple operation, good cycling performance, and not easy to cause harm to the environment. The high-efficiency adsorbent for printing and dyeing wastewater is the core issue of the adsorption.

In recent years, zero-valent iron (ZVI) nanoparticles with abundant REDOX active sites have received a lot of focus [10]. However, ZVI tends to accumulate in solution, which reduces its reactivity. Therefore, some porous materials are used to support ZVI to improve the stability of ZVI, such as activated carbon, zeolite, biochar, and so on. Nevertheless, the synthesis of ZVI composites is high-cost and low-load, and it is necessary to optimize ZVI composites. HC is a product prepared under high pressure and low temperature, with rich functional groups and porous structure [11,12], which shows great potential in removing pollution [13,14]. Hence, HC seems to be an ideal material to load ZVI. At present, the main sources of ZVI are  $K_3[Fe(C_2O_4)] \cdot 3H_2O$  [15] and  $FeCl_3 \cdot 6H_2O$  [16,17], reduced iron powder, and iron ores, which mainly includes limonite, siderite, and magnetite [18]. These materials have the disadvantages of complex preparation methods and high cost [19], although they have the advantages of environmental protection, economy, and efficient use [20,21]. The composite material of hydrochar and ZVI prepared with the above modifiers is at variance with the concept of sustainable development. Therefore, it is urgent to find new modified materials.

The accumulated stock of copper slag (CS) in China has reached 120 million tons [22], but the actual utilization of CS is rare. The iron in CS mainly exists in the form of weakly magnetic iron, and the effect of metal recovery by traditional methods is ineffective. The long-term and large accumulation of CS not only causes land occupation but also damages the soil and water environment [23]. Iron, copper, and other valuable metals are prevalent in CS, and it is worth noting that the iron content in CS ( $Fe\% = 35\%$ ) is significantly greater than that recovered from iron ore ( $Fe\% > 27\%$ ) [24]. Our research group has used CS as the modified material to prepare the relevant functional bio-adsorbent via the hydrothermal reduction method to remove heavy metal (Selenium) from the solution, and the absorption efficiency of the bio-adsorbent was great. However, whether the magnetic hydrochar modified by CS can be used in dye wastewater treatment and whether it can achieve cationic and anionic dyes elimination simultaneously remain to be studied. Moreover, the adsorption mechanism and industrial feasibility also need to be explored.

Therefore, in this research, we prepared magnetic hydrochar modified by CS and explored the removal efficiency of cationic dyes (methylene blue, MB) and anionic dyes (methyl orange, MO) in printing wastewater. The intention of this work was to obtain adsorbent magnetic hydrochar modified by CS via the hydrothermal reduction called CSHC and use CSHC for the adsorption of dyes. In this study, we believe that pine sawdust is used as the precursor to prepare hydrochar, and CS was innovatively modified with the help of high cellulose content and rich lignin in the structure. The combination of the two can not only effectively expand the specific surface area but the pore system of adsorbent materials. Moreover, the ZVI reduced in the preparation process could also be effectively attached to the hydrochar, thus providing a greater possibility for the adsorption of target pollutants. Therefore, the modified hydrochar was prepared by the one-pot method using CS as an iron source and pine sawdust as a carrier to explore its removal

efficiency of cationic dyes (methylene blue, MB) and anionic dyes (methyl orange, MO) in printing and dyeing wastewater is a promising solution. Modified hydrochar (CSHC) was prepared from copper slag and pine sawdust as a high-performance adsorbent and applied to the removal of MB and MO from printing and dyeing wastewater. Various characterization methods were used to investigate the physical and chemical properties of the prepared CSHCS before and after modification. The simultaneous removal of MB and MO was tested by batch adsorption experiments. Thermodynamic analysis and kinetic model were used to illustrate the surface interaction and adsorption types, respectively. The reusability of the composite functional environmental protection material was evaluated by a recycling test. All this work could provide a promising and potential solution for CS reutilization and wastewater purification.

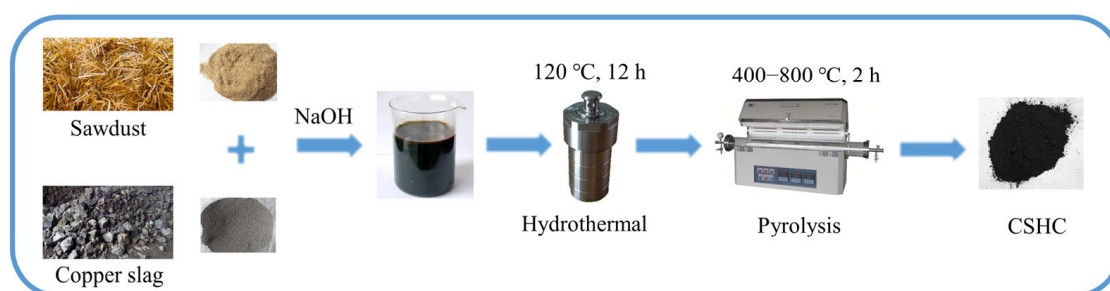
## 2. Resources and Techniques

### 2.1. Research Materials

The CS was obtained from Xuanwei Phoenix Steel Co, Ltd., from Qujing City, China. The pinewood sawdust was collected from Kunming City, China. The methylene blue ( $C_{16}H_{18}ClN_3S$ , solubility in water:  $40\text{ g}\cdot\text{L}^{-1}$  at  $25\text{ }^{\circ}\text{C}$ , molar mass:  $373.9\text{ g}\cdot\text{mol}^{-1}$ ), methyl orange ( $C_{14}H_{14}N_3NaO_3S$ , solubility in water:  $200\text{ mg}\cdot\text{L}^{-1}$  at  $25\text{ }^{\circ}\text{C}$ , molar mass:  $327.3\text{ g}\cdot\text{mol}^{-1}$ ), NaOH, and other reagents were provided from Beijing Chemical Reagent Factory. The pinewood SD was rinsed with distilled water and dried at  $80\text{ }^{\circ}\text{C}$ , and then the dried pinewood sawdust was crushed and passed through 80 mesh.

### 2.2. Adsorbent Preparation Methods

The preparation of CSHC is shown in Scheme 1 [25]. Firstly, weighed CS (4 g) and CS (4 g) were mixed. Secondly, the mixture was steeped in NaOH solution ( $200\text{ mg}\cdot\text{L}^{-1}$ , 40 mL) and distilled water (60 mL) in order to reduce the crystallinity of cellulose in SD and improve the mixing degree, and then it was mixed by ultrasonic oscillation ( $25\text{ }^{\circ}\text{C}$ , 0.5 h) and stirred by a magnetic stirring apparatus ( $25\text{ }^{\circ}\text{C}$ , 2 h). Thirdly, the mixture had a hydrothermal reaction ( $120\text{ }^{\circ}\text{C}$ , 10 h). Finally, the dried slurry was placed in a tube furnace and underwent a pyrolysis reaction (heating rate was  $10\text{ }^{\circ}\text{C}\cdot\text{min}^{-1}$ , pyrolysis temperature was 400, 600, or  $800\text{ }^{\circ}\text{C}$ , and holding time was 2 h,  $N_2$  protection). The three samples were washed with deionized water three times and were labeled CSHC400, CSHC600, and CSHC800, respectively. In addition, 8.0 g SD and 8.0 g CS were weighed and pyrolyzed (heating rate was  $10\text{ }^{\circ}\text{C}\cdot\text{min}^{-1}$ , pyrolysis temperature was  $600\text{ }^{\circ}\text{C}$ , and holding time was 2 h,  $N_2$  protection), respectively, and the products were labeled HC600 and CS600.



**Scheme 1.** Flowchart of preparation of CSHC.

### 2.3. Analysis Methods

The surface functional groups of the hydrochar were measured with Fourier transform infrared spectroscopy (FTIR, Spectrum Two, Perkin-Elmer, Waltham, MA, USA) using the KBr disk technique. Scanning electron microscopy (SEM, FEI Quanta 200FEG, Thermo Scientific Quanta, Hillsboro, OR, USA) was used to detect the surface morphology. The specific surface area (SSA) of biochar was detected by  $N_2$  adsorption isotherms at 77 K using a Micropore Analyzer (ASAP 2460, Micrometrics, Norcross, GE, USA). The crystal

structure was characterized by X-ray diffractometry (XRD, D8 Advance Sox-I, Bruker Co., Billerica, MA, USA) with Cu K-alpha radiation at 40 kV ( $\lambda = 0.15418$  nm). An X-ray photoelectron spectrometer (XPS, ESCALAB 250Xi, Thermo Fisher Scientific, Waltham, MA, USA) was used to characterize the surface composition and chemical state of the modified bone hydrochar before and after the adsorption of the organic dyes.

#### 2.4. Batch Experiment

All sorption experiments were performed in a 10 mL centrifuge tube with varied environmental factors at optimum operational parameters. The initial solution pH was adjusted with trace amounts of  $0.001\text{--}0.1\text{ mol}\cdot\text{L}^{-1}$  HCl/NaOH solutions. The adsorption kinetics were investigated by dispersing 10.0 mg of adsorbent into 10 mL of aqueous MB and MO solutions containing different initial concentrations (i.e., 50 or  $500\text{ mg}\cdot\text{L}^{-1}$ ) at pH = 12 for MB and pH = 3 for MO,  $T = 318\text{ K}$ . The adsorption isotherm experiments were carried out by vigorously shaking 10 mL of a solution containing varied levels of organic dyes (MB and MO from 25 to  $500\text{ mg}\cdot\text{L}^{-1}$ ) mixed with 10.0 mg of CSHC for 3 h to reach equilibrium at pH = 12.0 and pH = 3.0, respectively,  $T = 318\text{ K}$ .

Adsorption experiments were carried out in an orbital shaker (HNY-100B, Honour instrument shaker, Tianjin, China) at  $120\text{ rpm}\cdot\text{min}^{-1}$  for 3 h to ensure that the sorption reached equilibrium. The supernatants were then filtered with a  $0.22\text{ }\mu\text{m}$  filter membrane, followed by determining the MB and MO concentrations ( $C_e$ ,  $\text{mg}\cdot\text{L}^{-1}$ ) with an Ultraviolet-visible spectrophotometer (UV-722, Evolution 201 & 220, Thermo Fisher Scientific, Waltham, MA, USA) to measure the quantitative absorbance of these organic dyes under the influence of an adsorbent. Then, the MB and MO adsorption capacities of the adsorbent materials were computed. The MB was centered at a wavelength of 663 nm [26], and the MO was centered at a wavelength of 463 nm [27]. According to Formulas (1) and (2), the adsorption capacity  $q_e$  ( $\text{mg}\cdot\text{g}^{-1}$ ) and removal rate can be calculated, respectively. The calculation formula of the Langmuir model and Freundlich model was shown as Formulas (3) and (4). Additionally, Formulas (5) and (6) provided the expressions for the pseudo-first-order model and pseudo-second-order model. In order to ensure the uniformity of measurement and accuracy of dates, all experiments were repeated three times.

$$q_e = \frac{(C_0 - C_e) \times V}{W} \quad (1)$$

$$\text{Removal rate} = \frac{C_0 - C_e}{C_0} \times 100\% \quad (2)$$

where  $C_0$  ( $\text{mg}\cdot\text{L}^{-1}$ ) was the initial concentration of dye,  $C_e$  ( $\text{mg}\cdot\text{L}^{-1}$ ) was the concentration of dye solutions after adsorption,  $V$  (L) was the volume, and  $W$  (g) was the quantity of the adsorbent.

$$\text{Langmuir model : } q_e = \frac{q_m \cdot K_L \cdot C_e}{1 + K_L \cdot C_e} \quad (3)$$

$$\text{Freundlich model : } q_e = K_L \cdot C_e^{\frac{1}{n_F}} \quad (4)$$

where  $C_e$  ( $\text{mg}\cdot\text{L}^{-1}$ ) was the action's equilibrium content,  $q_e$  ( $\text{mg}\cdot\text{g}^{-1}$ ) was the target pollutant's absorption capacity,  $K_L$  ( $\text{L}\cdot\text{mg}^{-1}$ ) was the constant in the Langmuir model,  $K_F$  ( $\text{mg}^{1-n} \text{L}^n \cdot \text{g}^{-1}$ ) was the constant in the Freundlich model, and  $q_m$  ( $\text{mg}\cdot\text{g}^{-1}$ ) was the highest adsorbent capacity.

$$\text{Pseudo-first-order model : } q_t = q_e (1 - e^{-k_1 t}) \quad (5)$$

$$\text{Pseudo-second-order model : } q_t = \frac{q_e^2 k_2 t}{1 + q_e k_2 t} \quad (6)$$

The quantities of MB and MO that were adsorbed onto the CSHC600 at equilibrium and time  $t$ , respectively, are denoted by the variables  $q_e$  and  $q_t$  in these formulations,

whereas  $k_1$  ( $\text{min}^{-1}$ ) and  $k_2$  ( $\text{g} \cdot (\text{mg min})^{-1}$ ) were the constants for the pseudo-first-order and pseudo-second-order models, respectively. The fitting results are shown in Table 1. The final fitting results showed that during the adsorption of MB, the  $R^2$  of the pseudo-second-order model was superior to that of the pseudo-first-order model, demonstrating that chemical adsorption dominated. Moreover,  $k_2$  on MB ( $2.58 \times 10^{-2}$ ) was larger than  $k_2$  on MO ( $1.87 \times 10^{-4}$ ), indicating that the equilibrium time of adsorption of MB by CSHC600 was shorter than that of MO.

**Table 1.** Pore structure analysis of four activated carbons.

Sample	Specific Area ( $\text{m}^2 \cdot \text{g}^{-1}$ )	Pore Volume ( $\text{m}^3 \cdot \text{g}^{-1}$ )	Pore Size ( $\text{\AA}$ )
CSHC800	201.33	0.16	27.15
CSHC600	186.40	0.15	28.37
CSHC400	159.71	0.13	25.32
HC600	122.33	0.12	20.35

### 3. Findings and Discussion

#### 3.1. Adsorbent Material Characterization

SEM directly displayed the morphologic characteristics of HC composites. The morphologies of unmodified HC600 and CSHC600 are shown in Figure 1. It was obvious to observe the different morphologies of HC600 and CSHC600. Compared with CSHC600, HC600 had a more smooth surface and dense structure with the unobvious distribution of micropores [28]. The edges of HC600 were mainly broken sheets, and a few fibrous structures could be detected, which was likely due to the pyrolysis of structural fibers in the SD [29]. There were metallic luster and white particles on the surface of CSHC600, which was most likely ZVI. The existence of ZVI could be attributed to the magnetic nanoparticles ( $\text{Fe}_3\text{O}_4$ ) [30,31] and demonstrated that zero-valent iron effectively bonded to the surface of hydrochar [32]. In addition, some pores with different sizes were formed on the surface of CSHC600, which showed random and uneven characteristics in disorganized directions, a large number of irregular agglomeration spherical particles were attached, and a small number of micro and macro cracks appeared around the agglomeration particles, which may be the cross-linking process of multi-pore development [26]. It helped the dispersion and adsorption of dye. Compared with HC600, it was also noted that the pore diameters of CSHC600 were significantly reduced (Figure 1b). This phenomenon was due to the introduction of magnetite modifications, which blocked the pore.

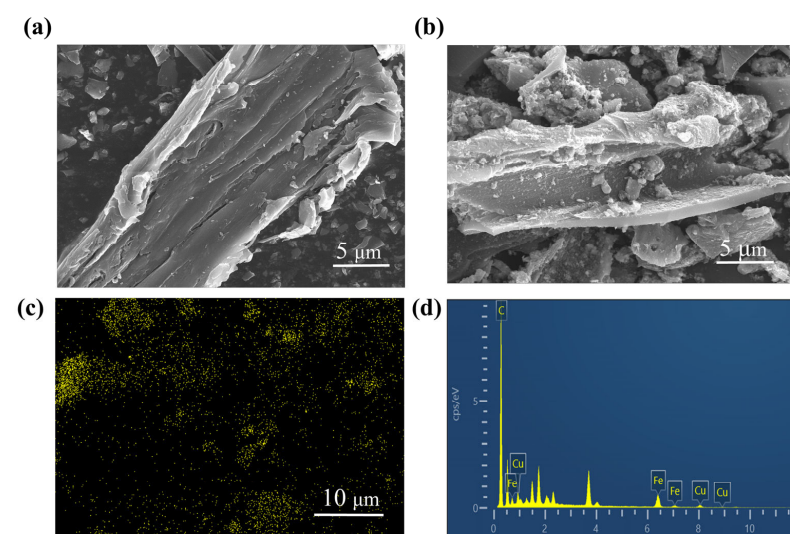


**Figure 1.** SEM images of HC600 (a) and SEM–EDS images of CSHC600 (b–d).



According to Figure 2, based on the IUPAC classification, CSHC is a typical Type I adsorption isotherm. When  $P/P^0 \leq 0.48$ , adsorption isotherms coincide with desorption isotherms, indicating that activated carbon has a microporous structure. With the increase of pressure, capillary condensation occurs in the pore structure, and the desorption rate of  $N_2$  is higher than the adsorption rate, and H4-type hysteresis rings are produced, indicating the existence of a mesoporous structure. Such microporous mesopores not only provide more adsorption sites but also improve the adsorption rate. The formation of pores is caused by the dehydration of hydrochar. Surface materials begin to aggregate and form granular microcarbon balls. There are pores of different sizes inside and between the particles. Table 1 shows that the specific surface area of CSHC600 and HC600 are  $186.40 \text{ m}^2 \cdot \text{g}^{-1}$  and  $122.33 \text{ m}^2 \cdot \text{g}^{-1}$ , respectively, and the total pore volume is  $0.15 \text{ m}^3 \cdot \text{g}^{-1}$  and  $0.12 \text{ m}^3 \cdot \text{g}^{-1}$ , indicating that the pore structure and  $S_{\text{BET}}$  are improved by about 1.52 times after CS modification.  $V_{\text{tot}}$  improved by about 1.25 times. This shows that CS-modified hydrochar can be a very good preparation of high specific surface area adsorbent.

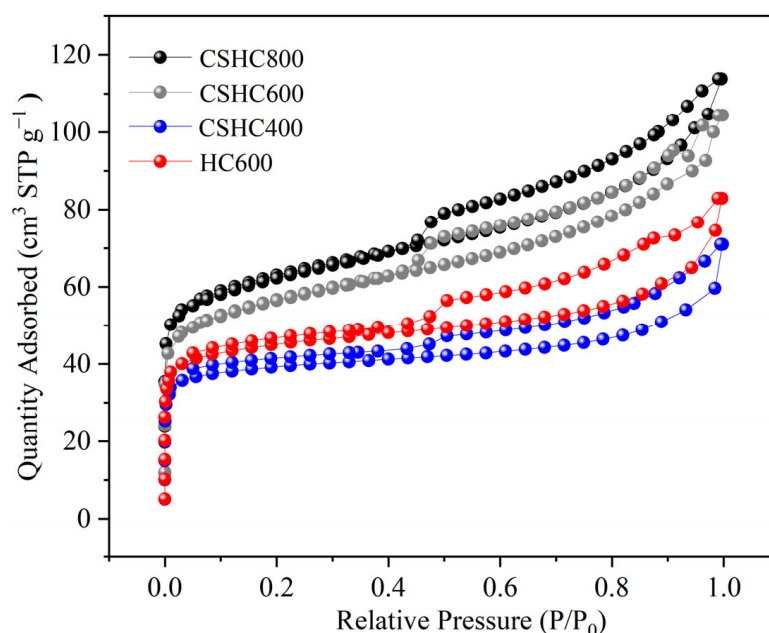


**Figure 2.**  $N_2$  adsorption/desorption isotherms of four activated carbons.

The XRD diffractograms of HC600 and CS600 are shown in Figure 3. There was an intense peak corresponding to  $\text{SiO}_2$  at  $2\theta$  of  $26.66^\circ$ , and there were diffraction peaks of  $\text{CaCO}_3$  at  $2\theta$  of  $20.95^\circ$  and  $29.56^\circ$ . In the XRD diffractograms of CSHC, there were diffraction peaks of  $\text{Fe}^0$  and  $\text{Fe}_3\text{O}_4$  at  $2\theta$  of  $44.57^\circ$ ,  $35.47^\circ$ , and  $57.54^\circ$ , respectively. The diffraction peak at  $2\theta = 46.81^\circ$  represented  $\text{Cu}_5\text{FeS}_4$ , and the appearance of  $\text{Cu}_5\text{FeS}_4$  may be the result of a high-temperature vulcanization reaction between copper, iron, and residual sulfur in CS during the pyrolysis process [33]. Compared HC600 to CSHC600,  $\text{Fe}^0$  and  $\text{Fe}_3\text{O}_4$  were successfully attached to the surface of the modified hydrochar [34]. In addition, when the temperature rose, the peak intensity of  $\text{Fe}^0$  rose. This was because more reducing gases were created at high temperatures, which reduced  $\text{Fe}^{2+}$  and  $\text{Fe}^{3+}$  into  $\text{Fe}^0$ .

In the FTIR spectra (Figure 2b), the wide peaks at  $3435 \text{ cm}^{-1}$  and  $877 \text{ cm}^{-1}$  [35] represented the O–H and C–H, and the oscillation peak at  $1647 \text{ cm}^{-1}$  and  $1008 \text{ cm}^{-1}$  represented C=O [36,37], and the peak at  $1065 \text{ cm}^{-1}$  represented Si–O–Si [38]. The FTIR spectra showed the presence of functional groups such as –OH ( $3429 \text{ cm}^{-1}$ ), C=O ( $1008 \text{ cm}^{-1}$ ), C–H ( $1647 \text{ cm}^{-1}$ ), C=C ( $1426 \text{ cm}^{-1}$ ), and so on in these adsorbents.

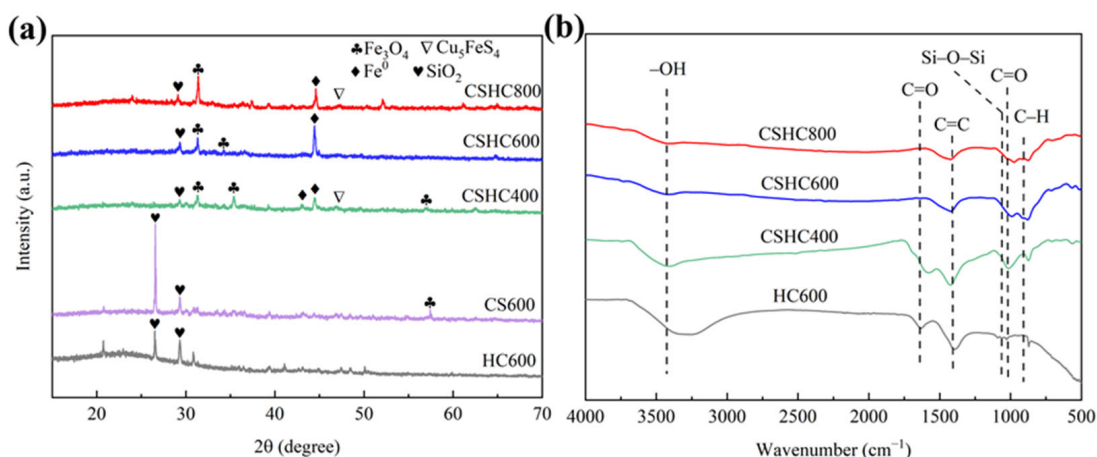


**Figure 3.** (a,b) XRD diffractograms and FTIR spectra of CSHC, CS600, and HC600.

In addition, it was observed that the oxygen-rich functional groups in the modified hydrochar prepared by pyrolysis at 600 °C and 800 °C were more than adsorbent prepared by pyrolysis at 400 °C. This indicated that pyrolysis at 600 °C stimulated and retained oxygen-rich functional groups and aromatic substances better [38], and thus CSHC600 had a better effect on the adsorption of MB and MO.

The XPS analysis is shown in Figure 4. The binding energy at 288.1 eV and 529.1 eV represented C 1s and O 1s, respectively, and the binding energy at 348.3 eV represented Ca 2p. The peaks at 710.13 eV and 725.14 eV represented  $\text{Fe}^{2+}$ , moreover, the peaks at 711.26 eV and 727.24 eV represented  $\text{Fe}^{3+}$ . The peaks at 720.10 eV represented  $\text{Fe}^0$ , indicating that  $\text{Fe}^0$  was successfully loaded onto HC [39,40].

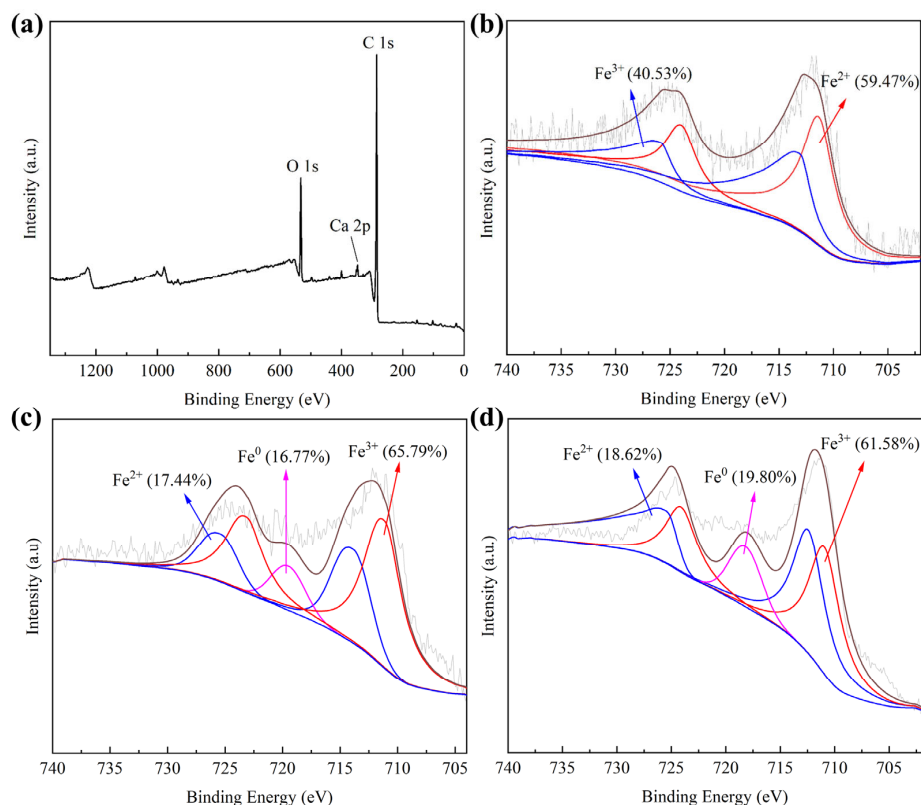


**Figure 4.** The full spectrum of CSHC600 (a) and XPS images of CSHC400 (b), CSHC600 (c), and CSHC800 (d).

The magnetic properties of CSHC400, CSHC600, and CSHC800 were determined by a vibrating sample magnetometer with a pole diameter of 5 cm under the condition of 300 K. The magnetic effect of zero-valent iron modified hydrochar was prepared from copper residue. The saturation magnetic strength of CSHC600 was  $79.83 \text{ emu} \cdot \text{g}^{-1}$ , while that of CSHC400 and CSHC800 were  $62.60 \text{ emu} \cdot \text{g}^{-1}$  and  $60.92 \text{ emu} \cdot \text{g}^{-1}$ , respectively (Figure 5). Thus, the high-temperature pyrolysis magnetized the hydrochar [41], but the magnetization did not change with temperature. The intensity of magnetization was related to the generation of  $\text{Fe}_3\text{O}_4$  during pyrolysis, and  $\text{Fe}_3\text{O}_4$  had a high conductivity [42]. The adsorption properties were usually due to the electron transfer of ferromagnetism (ferrite magnets) between  $\text{Fe}^{2+}$  and  $\text{Fe}^{3+}$ . A secondary phase transition occurred above the Curie temperature to a paramagnetic substance. Due to the Curie temperature of  $\text{Fe}_3\text{O}_4$  being  $585^\circ\text{C}$ , the pyrolytic temperature of  $600^\circ\text{C}$  can oxidize the iron part of CS to  $\text{Fe}_3\text{O}_4$  to the greatest extent. The stronger the magnetic properties of the adsorbent, the more favorable the magnetization separation between the adsorbent and the dyeing wastewater [43]. Under the attraction of a permanent magnet, the adsorbent can be quickly separated from the adsorption liquid. Considering the adsorption capacity and magnetic properties, CSHC600 was considered the optimal one for further analysis.

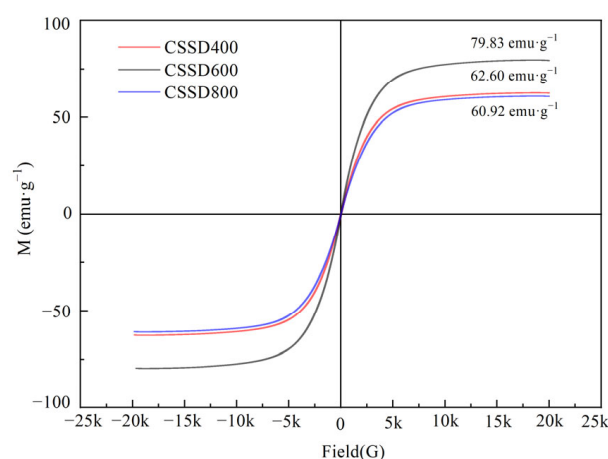


**Figure 5.** VSM spectra of CS600, CSHC400, CSHC600, and CSHC800.

### 3.2. Analysis of Batch Experiments

#### 3.2.1. Effect of pH

Figure 6 shows the effect of pH value on the adsorption capacity of CSHC600. The initial concentration of MB was  $50 \text{ mg} \cdot \text{L}^{-1}$ , the initial concentration of MO was  $500 \text{ mg} \cdot \text{L}^{-1}$ , and the pH of the solution was 3–12. When  $\text{pH} > 3$ , the adsorption capacity of CSHC600 for MB was high, but the overall trend was stable. When  $\text{pH} = 10$ , the adsorption capacity increased slightly. The results showed that CSHC600 can remove MB over a wide pH range. For MO, the maximum adsorption capacity appeared when  $\text{pH} = 3$ , but the adsorption capacity evidently decreased with the increase of pH value. This was probably due to  $\text{pH}_{\text{pzc}}$  6.42. The positive charge of protonation of functional groups on the surface of CSHC600 led to positive zeta potential, and the anionic dye MO can be adsorbed by electrostatic adsorption. As can be seen from Figure 6, the adsorbent had a strong adsorption capacity for MB under an alkaline environment and MO under an acidic environment [44]. According to previous studies, the adsorption effect of CS-derived zero-valent iron-modified hydrochars on MB and MO solutions varies significantly at different pH levels [45]. In addition, the pH of the adsorbed solution was measured, and it was found that for MB, the pH level varied from 2.8 to 11.2. Similarly, the pH of MO varies from 3.5 to 11.8. The reason for this result may be that electrostatic attraction neutralizes part of the charge in the adsorption process, making the solution nearly neutral. However, the adsorbent material itself shows alkalinity, so most of the solution after adsorption is weak alkalinity, while the individual shows strong alkalinity.



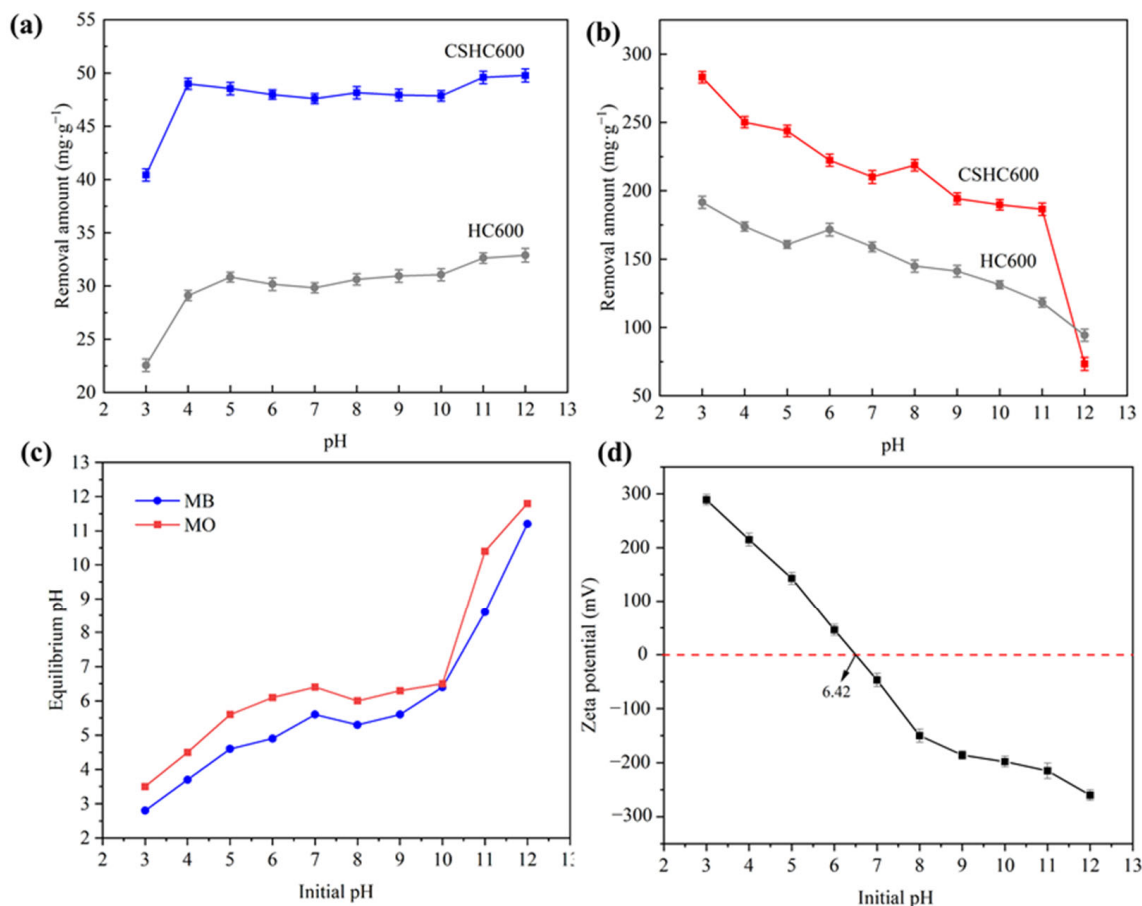


**Figure 6.** MB (a) and MO (b) were adsorbed onto CSHC600 and HC600 at various pH levels; Solution pH after adsorption of MB and MO (c); Zeta potential determination (d). Experiment conditions: [dosage = 1 g·L<sup>-1</sup>], [temperature = 318 K], [MB = 50 mg·L<sup>-1</sup>], [MO = 500 mg·L<sup>-1</sup>], [reaction time = 3 h].

### 3.2.2. Analysis of Isothermal Adsorption

The adsorption efficiency of CSHC600 on MB and MO at various initial concentrations are shown in Figure 7c,d, and the similarities between MB and MO were obvious. The adsorption capacity gradually rose as the pollutant concentration rose. The adsorption capacity of CSHC600 tended to be steady when the concentration rose to a certain point. The experimental dates were fitted by the Langmuir and Freundlich models [46], and the results are shown in Table 2. For the adsorption MB by CSHC600, the  $R^2$  of the Langmuir model was considerably higher (0.99) than that of the Freundlich model (0.94). For the adsorption MO by CSHC600,  $R^2$  values were 0.97 and 0.88 for the Langmuir and Freundlich models, respectively. Thus, the MB and MO absorption process was better fitted by the Langmuir model [47]. The statement of Langmuir has four basic assumptions. There is no interaction between substrates, there is no adsorption site with the same energy, all adsorption sites are equivalent, and the substrate is uniformly distributed on the surface of the adsorbent monolayer film [48,49]. In other words, the adsorption preponderance of MB and MO by CSHC600 was mediated by chemisorption on a single molecular layer [50,51]. CSHC600 was an effective MB and MO adsorbent, which showed the best effect [52], as its greatest adsorption capacity respectively reached 278.21 mg·g<sup>-1</sup> and 357.02 mg·g<sup>-1</sup> for MB and MO (Table 2), which compared with other research data (Table 3). These results show that CSHC600 was an effective substance for removing these two kinds of organic dyes.

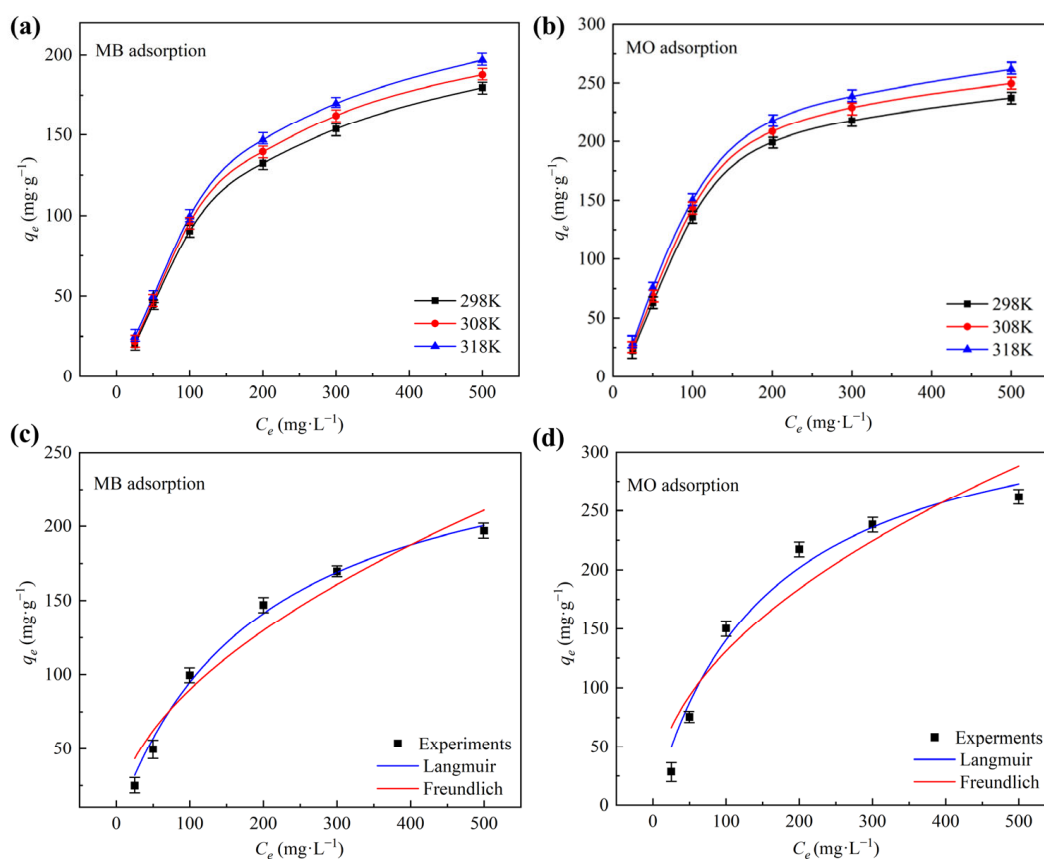


**Figure 7.** The MB (a) and MO (b) removal capacities of the isotherms, thermodynamics (c); Fitted curves of MB (c) and MO (d) for the Langmuir and Freundlich isotherms. Experiment conditions: [dosage = 1 g·L<sup>-1</sup>], [temperature = 318 K], [MB = 50 mg·g<sup>-1</sup>], [MO = 500 mg·g<sup>-1</sup>], [reaction time = 3 h].

**Table 2.** Adsorption isotherms, kinetics, and related factors summarized.

Isotherms	Target	Experimental Data	Parameters		R <sup>2</sup>
Langmuir			$q_m$ (mg·g <sup>-1</sup> )	$K_L$ (L·mg <sup>-1</sup> )	
	MB	196.89	278.21	0.005	0.99
	MO	261.78	357.02	0.006	0.97
Freundlich			$K_F$ (mg <sup>1-n</sup> L <sup>n</sup> ·g <sup>-1</sup> )	$1/n$	
	MB	196.89	7.80	0.53	0.94
	MO	261.78	13.68	0.49	0.88
Kinetics	Target	Experimental data	Parameters		
Pseudo-first-order			$q_e$ (mg·g <sup>-1</sup> )	$k_1$ (min <sup>-1</sup> )	
	MB	49.95	48.56	0.43	0.99
	MO	254.38	250.65	0.04	0.99
Pseudo-second-order			$q_e$ (mg·g <sup>-1</sup> )	$k_2$ (g·(mg·min) <sup>-1</sup> )	
	MB	49.95	49.52	$2.58 \times 10^{-2}$	0.99
	MO	254.38	287.14	$1.87 \times 10^{-4}$	0.99

**Table 2.** *Cont.*

Isotherms	Target	Experimental Data	Parameters		R <sup>2</sup>
Thermodynamics	T (K)	$\Delta G^0$ (KJ·mol <sup>−1</sup> )	$\Delta S^0$ (KJ·(mol·K) <sup>−1</sup> )	$\Delta H^0$ (KJ·(mol·K) <sup>−1</sup> )	
MB	298	−2.74	$1.96 \times 10^{-2}$	2.13	
	308	−3.68			
	318	−4.10			
MO	298	−4.85	$3.11 \times 10^{-2}$	3.87	
	308	−5.78			
	318	−6.02			

**Table 3.** Comparison of different magnetic hydrochar or biomass-based adsorbents' abilities to bind MB and MO.

Sample	Dosage (g·L <sup>−1</sup> )	pH	Initial Concentration (mg·L <sup>−1</sup> )	Capacity (mg·g <sup>−1</sup> )		
				MB	MO	
Fe <sub>3</sub> O <sub>4</sub> -PAMH	0.8	11 for MB 5 for MO	100	148.84	202.02	[53]
BM	0.5	7	50	2	41.49	[54]
NFGPBC	0.7	7	50	67.54	-	[55]
Asph-Al	10	3	20	-	41.25	[56]
FE-LB	2	4	200	180.00	-	[57]
CSHC600	1	12 for MB 3 for MO	50 for MB 500 for MO	49.58	261.78	This study

### 3.2.3. Adsorption Kinetics

Response time was also a key parameter in adsorption, which reflected the adsorption speed. Response time contributed to the efficient removal of pollutants and provided more valuable information for the adsorption process. According to the existing experimental data, CSHC600 had the best adsorption capacities for MB and MO when pH = 12 and pH = 3, respectively. The results of the fitting are displayed in Figure 8a,b. The adsorption equilibrium for MO was 130 min, and the adsorption equilibrium for MB was 30 min. The adsorption capacity of MO and MB increased rapidly during the early stages of adsorption, increased slowly, and ultimately tended to a stable state. MB and MO rapidly diffused from the solution to the surface of the adsorbent material, after that, the adsorption tended to be slow. There may have been a lot of adsorption active sites on the surface of CSHC600, but when the reaction was going on, these active sites gradually filled with small molecules such as MO and MB, which weakened the adsorption.

### 3.2.4. Thermodynamic analysis

Thermodynamic analysis was carried out by evaluating the entropy and energy changes in the adsorption process. The formula for figuring out the Gibbs free energy and other factors during the adsorption process is shown in Formulas (7) and (8).

$$\ln\left(\frac{q_m}{C_e}\right) = \frac{\Delta S^0}{R} - \frac{\Delta H^0}{RT} \quad (7)$$

$$\Delta G^0 = \Delta H^0 - T\Delta S^0 \quad (8)$$

where  $\Delta G^0$  represented the change in free energy,  $\Delta S^0$  represented the change in entropy, and  $\Delta H^0$  represented the change in enthalpy. The isothermal adsorption data were used to calculate  $\ln\left(\frac{q_m}{C_e}\right)$ , which had been given a value of  $8.314 \text{ J} \cdot (\text{mol} \cdot \text{K})^{-1}$  [58], where T was the temperature and R was the universal gas constant.

Table 2 showed that  $\Delta G^0$  adsorbing MB by CSHC600 at 318 K was  $-4.10 \text{ KJ}\cdot\text{mol}^{-1}$ , while that of MO was  $-6.02 \text{ KJ}\cdot\text{mol}^{-1}$ . Both  $\Delta G^0$  values were negative when adsorbing MB and MO, indicating that the adsorption reactions may be totally irreversible [59]. The  $\Delta H^0$  was positive, indicating the reactions were endothermic.

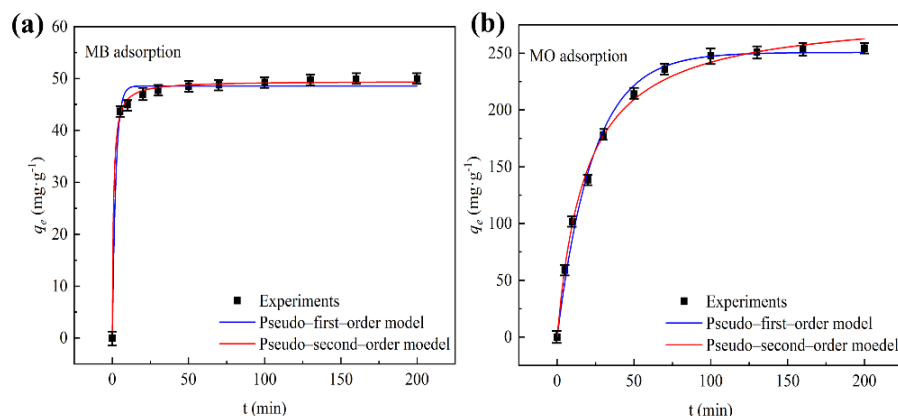


**Figure 8.** The adsorption kinetics of MB (a) and MO (b). Fitting of adsorption kinetics by linear relations of pseudo-first-order and pseudo-second-order models.

### 3.3. Regeneration Experiments

CSHC600 was a reusable adsorbent (Figure 9). Solvent desorption was used to evaluate the reproducibility of CSHC. The main method was achieved through five continuous adsorption-desorption processes [47]. To achieve pH neutrality, the attachments of the adsorbent were eluted, and the residue was repeatedly rinsed with deionized water. The recovered adsorbent was dried in a vacuum drying oven at  $60^\circ\text{C}$ . To explore regeneration capabilities, the adsorption was placed into the same adsorption circumstances as previously, and the adsorption-desorption cycle was carried out five times. By using CSHC600, MB ( $50 \text{ mg}\cdot\text{L}^{-1}$ ) and MO ( $500 \text{ mg}\cdot\text{L}^{-1}$ ) can be reused with ease. As shown in Figure 10, MB could almost be desorbed completely. The removal rate of CSHC600 on MB was still achieved at 97% after five cycles. At pH = 3, the removal rate of MO by CSHC600 was 51% in the first cycle and more than 41% in the fifth cycle. The removal rates of CSHC600 for MB and MO were great even after five cycles. The decrease in adsorption efficiency may be related to the fact that some original adsorption sites of CSHC600 were occupied and did not regenerate after the preliminary test. The removal rates of CSHC600 for MB and MO were great even after five cycles. The outcomes demonstrate that CSHC600 was simple to recycle and has strong adsorption capability.

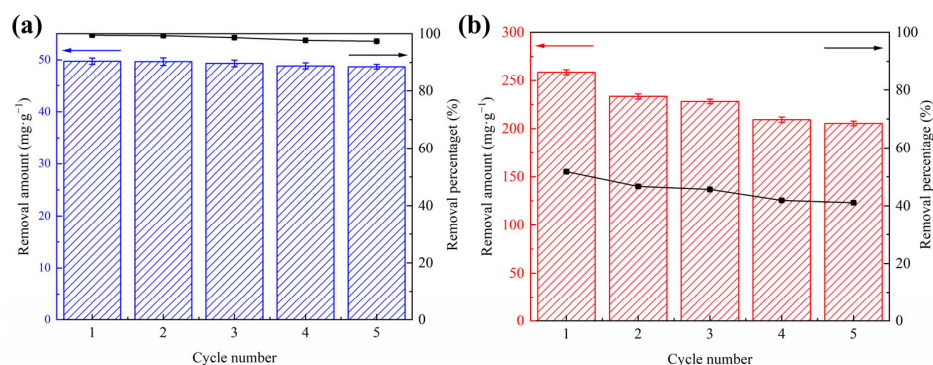


**Figure 9.** Adsorption of MB (a) and MO (b) using CSHC600 as an adsorbent that is reusable. Experiment conditions: [dosage =  $1 \text{ g}\cdot\text{L}^{-1}$ ], [temperature = 318 K], [MB =  $50 \text{ mg}\cdot\text{g}^{-1}$ ], [MO =  $500 \text{ mg}\cdot\text{g}^{-1}$ ], [reaction time = 3 h].

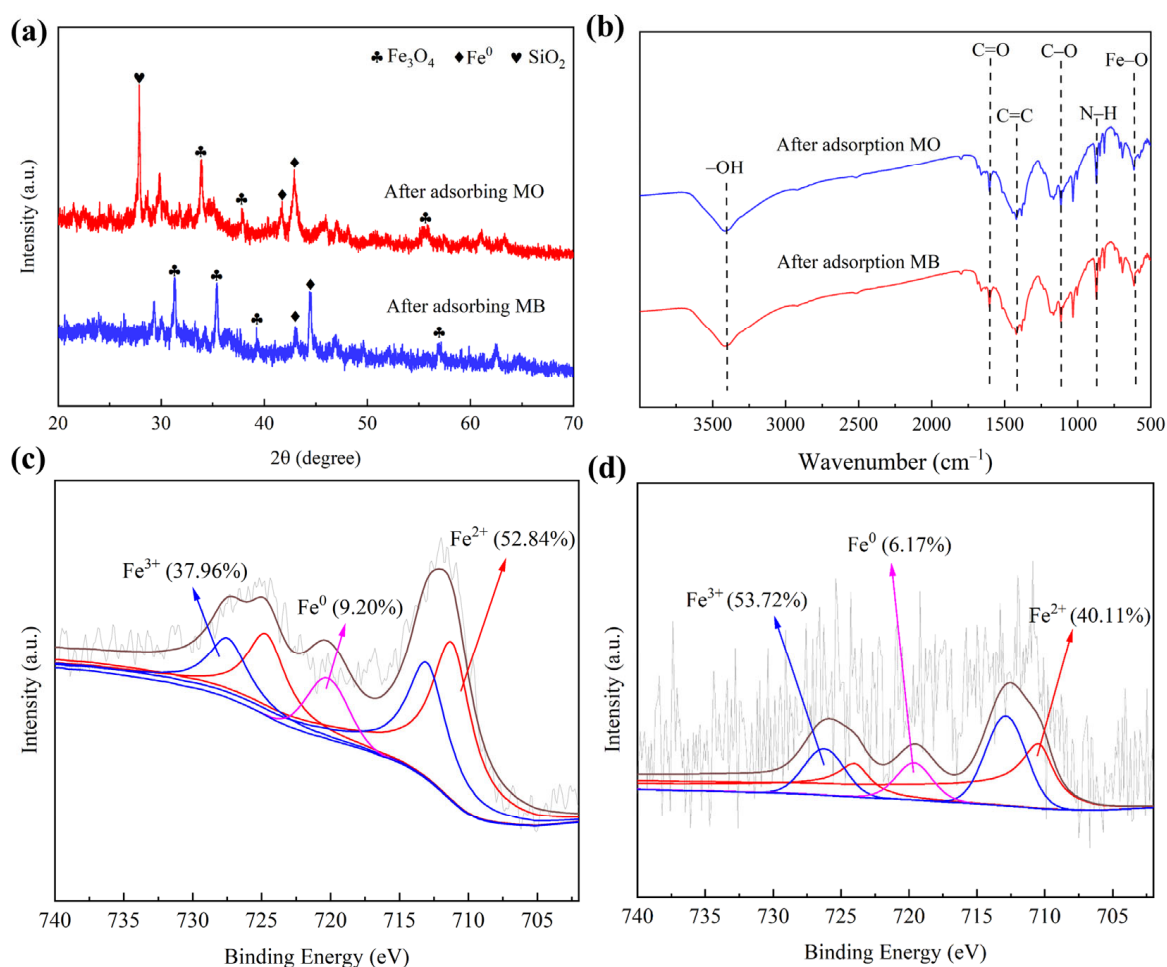


**Figure 10.** The images of XRD, FTIR, and XPS of CSHC600 after adsorption. (a) XRD diffractograms, (b) FTIR spectra, (c) XPS of CSHC600 adsorption of MB, (d) XPS of CSHC600 adsorption of MO.

### 3.4. Mechanisms

The removal mechanisms of MB and MO were studied. The SEM images showed that CSHC600 had a smooth surface and uniform pore distribution. In addition, the crystal structure of the adsorbent was discovered. The FTIR spectra after adsorption (Figure 10) showed that the interaction of these functional groups on the surface of CSHC600 with MB and MO, for example,  $-\text{OH}$  and  $-\text{COOH}$  functional groups shifted, the strength of  $\text{C}-\text{C}$  functional groups decreased, and additionally  $\text{C}-\text{O}$  and  $-\text{COOH}$  participated in the reaction. This indicated that hydrogen bonding existed in the adsorption process of CSHC600 [60]. By comparing the XRD diffractograms of CSHC before and after adsorption, it can be seen that  $\text{Fe}^0$  decreased obviously after adsorption. It was also clear that the peak of  $\text{Fe}^0$  significantly weakened after adsorption, which may be because ZVI loaded on CSHC600 reduced mineralized MB and MO. Eventually, the dye was degraded to small molecules such as  $\text{CO}_2$  and  $\text{H}_2\text{O}$ , while ZVI was oxidized to  $\text{Fe}^{2+}$  and  $\text{Fe}^{3+}$ . As MO was a typical anionic compound, the positive and negative charges between  $\text{Fe}^{2+}$ ,  $\text{Fe}^{3+}$ , and MO attracted each other, which attached MO to the surface of the adsorbent. According to the XPS of CSHC before and after adsorption, the peak of  $\text{Fe}^{3+}$  increased significantly after adsorption. A large amount of  $\text{Fe}^{3+}$  flocculated with the free  $-\text{OH}$  in solution to form  $\text{Fe}(\text{OH})_3$ . Precipitation was the main mechanism of dye adsorption by hydrochar. In the same way, HC was usually alkaline and carried a negative charge, which can be well combined with cationic dye (MB) via complexation (Figure 11).



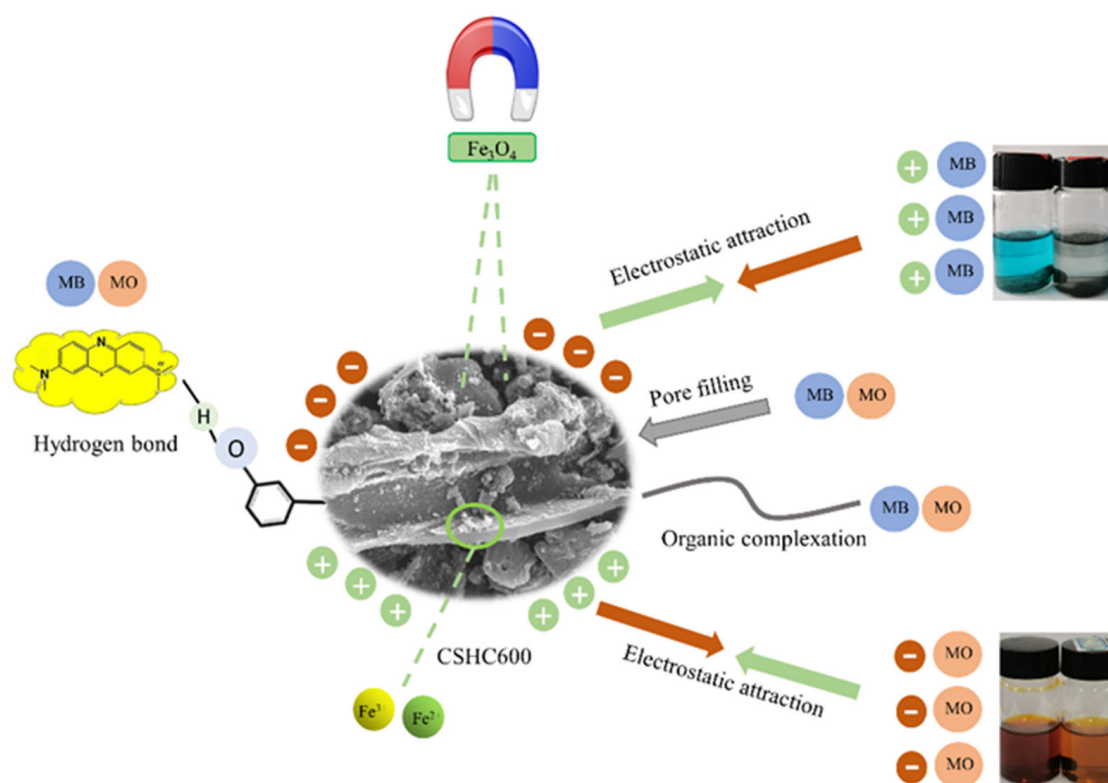


**Figure 11.** Adsorption mechanism of MO and MB by CSHC.

#### 4. Conclusions

In this work, the green construction of CSHC was realized by the hydrothermal method with pine sawdust as a carrier and copper slag as an iron source. A variety of characterization methods have demonstrated the successful loading of ZVI. The adsorption process of CSHC600 on MB and MO was fitted by the pseudo-second-order kinetic equation and Langmuir model, respectively. The adsorption process is mainly controlled by chemisorption, and the maximum adsorption capacity is  $278.21 \text{ mg}\cdot\text{g}^{-1}$  and  $357.02 \text{ mg}\cdot\text{g}^{-1}$ , respectively. CSHC600 has good recovery performance. The experimental results prove the feasibility of copper slag and pine chip adsorbent for purifying industrial wastewater containing cationic dyes and anionic dyes.

**Author Contributions:** H.W.: Conceptualization; Y.W. (Yi Wu): Formal Analysis, Writing—Original Draft; Y.W. (Yi Wen): Data Curation, Software, Methodology; D.C.: Data Curation, Investigation, Methodology; J.P.: Supervision; Y.D.: Supervision; S.K.: Conceptualization; S.W.: Writing—Review & Editing; R.X.: Funding Acquisition, Resources, Supervision, Supervision, Writing—Review & Editing. All authors have read and agreed to the published version of the manuscript.

**Funding:** This research was supported by the Applied Basic Research Foundation of Yunnan Province (202201AS070020, 202201AU070061, 202101AU070008), Yunnan Province Education Department Project (2022J0136), Yunnan Academy of Experts Workstation (Xurui Shiping Workstation).

**Institutional Review Board Statement:** Not applicable.

**Data Availability Statement:** Not applicable.

**Conflicts of Interest:** This paper is an original work of the authors who have read and approved this version, and due care has been taken to ensure the integrity of the work. No part of this paper has been published or submitted elsewhere. No conflict of interest exists in the submission of this manuscript. A statement explaining why the manuscript is novel and significant is stated below.

## References

- Shao, Q.; Li, Y.; Wang, Q.; Niu, T.; Li, S.; Shen, W. Preparation of copper doped walnut shell-based biochar for efficiently removal of organic dyes from aqueous solutions. *J. Mol. Liq.* **2021**, *336*, 116314. [\[CrossRef\]](#)
- Shaikh, W.A.; Chakraborty, S.; Islam, R.U.; Ghfar, A.A.; Naushad, M.; Bundschuh, J.; Maity, J.P.; Mondal, N.K. Fabrication of biochar-based hybrid Ag nanocomposite from algal biomass waste for toxic dye-laden wastewater treatment. *Chemosphere* **2022**, *289*, 133243. [\[CrossRef\]](#) [\[PubMed\]](#)
- Sutar, S.; Patil, P.; Jadhav, J. Recent advances in biochar technology for textile dyes wastewater remediation: A review. *Environ. Res.* **2022**, *209*, 112841. [\[CrossRef\]](#) [\[PubMed\]](#)
- Gao, Y.; Zhang, J.; Chen, C.; Du, Y.; Teng, G.; Wu, Z. Functional biochar fabricated from waste red mud and corn straw in China for acidic dye wastewater treatment. *J. Clean. Prod.* **2021**, *320*, 128887. [\[CrossRef\]](#)
- Sun, Y.; Wang, T.; Han, C.; Bai, L.; Sun, X. One-step preparation of lignin-based magnetic biochar as bifunctional material for the efficient removal of Cr(VI) and Congo red: Performance and practical application. *Bioresour. Technol.* **2023**, *369*, 128373. [\[CrossRef\]](#)
- Gautam, R.K.; Mandavi, G.M.; Mishra, R.K.; Chaturvedi, P.; Awashthi, M.K.; Singh, R.K.; Giri, B.S.; Pandey, P. Biochar for remediation of agrochemicals and synthetic organic dyes from environmental samples: A review. *Chemosphere* **2021**, *272*, 129917. [\[CrossRef\]](#)
- Cheng, H.; Liu, Y.; Li, X. Adsorption performance and mechanism of iron-loaded biochar to methyl orange in the presence of Cr<sup>6+</sup> from dye wastewater. *J. Hazard. Mater.* **2021**, *415*, 125749. [\[CrossRef\]](#)
- Cheng, C.; Liu, B.; Liu, C.; Shen, J.; Nurlan, J.; Khan, M.F.S.; Huang, Z.; Qian, Y.; Shen, F.; Wu, J. Tracking variation of fluorescent dissolved organic matter during full-scale printing and dyeing wastewater treatment. *Chemosphere* **2020**, *252*, 126559. [\[CrossRef\]](#)
- Chen, Y.; Ma, R.; Pu, X.; Fu, X.; Ju, X.; Arif, M.; Yan, X.; Qian, J.; Liu, Y. The characterization of a novel magnetic biochar derived from sulfate-reducing sludge and its application for aqueous Cr(VI) removal through synergistic effects of adsorption and chemical reduction. *Chemosphere* **2022**, *308*, 136258. [\[CrossRef\]](#)
- Li, X.; Xu, J.; Luo, X.; Shi, J. Efficient adsorption of dyes from aqueous solution using a novel functionalized magnetic biochar: Synthesis, kinetics, isotherms, adsorption mechanism, and reusability. *Bioresour. Technol.* **2022**, *360*, 127526. [\[CrossRef\]](#)
- Madduri, S.; Elsayed, I.; Hassan, E.B. Novel oxone treated hydrochar for the removal of Pb(II) and methylene blue(MB) dye from aqueous solutions. *Chemosphere* **2020**, *260*, 127683. [\[CrossRef\]](#)
- Tan, X.; Zhang, C.; Wei, H.; Shi, P.; Chang, H.; Ho, S. Versatile strategy of sulfanilamide antibiotics removal via microalgal biochar: Role of oxygen-enriched functional groups. *Chemosphere* **2022**, *304*, 135244. [\[CrossRef\]](#)
- Duan, L.; Wang, Q.; Li, J.; Wang, F.; Yang, H.; Guo, B.; Hashimoto, Y. Zero valent iron or Fe<sub>3</sub>O<sub>4</sub>-loaded biochar for remediation of Pb contaminated sandy soil: Sequential extraction, magnetic separation, XAFS and ryegrass growth. *Environ. Pollut.* **2022**, *308*, 119702. [\[CrossRef\]](#)
- Hou, Y.; Liang, Y.; Hu, H.; Tao, Y.; Zhou, J.; Cai, J. Facile preparation of multi-porous biochar from lotus biomass for methyl orange removal: Kinetics, isotherms, and regeneration studies. *Bioresour. Technol.* **2021**, *329*, 124877. [\[CrossRef\]](#)
- Zhang, X.; Tran, H.N.; Liu, Y.; Yang, C.; Zhang, T.; Guo, J.; Zhu, W.; Ahmad, M.; Xiao, H.; Song, J. Nitrogen-doped magnetic biochar made with K<sub>3</sub>[Fe(C<sub>2</sub>O<sub>4</sub>)<sub>3</sub>] to adsorb dyes: Experimental approach and density functional theory modeling. *J. Clean. Prod.* **2023**, *383*, 135527. [\[CrossRef\]](#)
- Ren, Z.; Wang, Z.; Lv, L.; Ma, P.; Zhang, G.; Li, Y.; Qin, Y.; Wang, P.; Liu, X.; Gao, W. Fe-N complex biochar as a superior partner of sodium sulfide for methyl orange decolorization by combination of adsorption and reduction. *J. Environ. Manag.* **2022**, *316*, 115213. [\[CrossRef\]](#)
- Chu, J.-H.; Kang, J.-K.; Park, S.-J.; Lee, C.G. Application of magnetic biochar derived from food waste in heterogeneous sono-Fenton-like process for removal of organic dyes from aqueous solution. *J. Water Process Eng.* **2020**, *37*, 101455. [\[CrossRef\]](#)
- Zhang, H.; Xue, G.; Chen, H.; Li, X. Magnetic biochar catalyst derived from biological sludge and ferric sludge using hydrothermal carbonization: Preparation, characterization and its circulation in Fenton process for dyeing wastewater treatment. *Chemosphere* **2018**, *191*, 64–71. [\[CrossRef\]](#)
- Chanda, P.T.; Pritam, S.; Nikoloski, N.A. The potential for copper slag waste as a resource for a circular economy: A review—Part II. *Miner. Eng.* **2021**, *172*, 107150.
- Shi, G.; Liao, Y.; Su, B.; Zhang, Y.; Wang, W.; Xi, J. Kinetics of copper extraction from copper smelting slag by pressure oxidative leaching with sulfuric acid. *Sep. Purif. Technol.* **2020**, *241*, 116699. [\[CrossRef\]](#)
- Zhou, W.; Liu, X.; Lyu, X.; Gao, W.; Su, H.; Li, C. Extraction and separation of copper and iron from copper smelting slag: A review. *J. Clean. Prod.* **2022**, *368*, 133095. [\[CrossRef\]](#)
- Chanda, P.T.; Pritam, S.; Nikoloski, N.A. The potential for copper slag waste as a resource for a circular economy: A review—Part I. *Miner. Eng.* **2022**, *180*, 107474.
- Yan, J.; Zuo, X.; Yang, S.; Chen, R.; Cai, T.; Ding, D. Evaluation of potassium ferrate activated biochar for the simultaneous adsorption of copper and sulfadiazine: Competitive versus synergistic. *J. Hazard. Mater.* **2022**, *424*, 127435. [\[CrossRef\]](#) [\[PubMed\]](#)
- Du, J.; Zhang, F.; Hu, J.; Yang, S.; Liu, H.; Wang, H. Direct reduction of copper slag using rubber seed oil as a reductant: Iron recycling and thermokinetics. *J. Clean. Prod.* **2022**, *363*, 132546. [\[CrossRef\]](#)
- Wang, H.; Cai, J.; Liao, Z.; Jawad, A.; Iftikhar, J.; Chen, Z.; Chen, Z. Black liquor as biomass feedstock to prepare zero-valent iron embedded biochar with red mud for Cr(VI) removal: Mechanisms insights and engineering practicality. *Bioresour. Technol.* **2020**, *311*, 123553. [\[CrossRef\]](#)

26. Bashir, A.; Pandith, A.H.; Qureashi, A.; Malik, L.A.; Gani, M.; Perez, J. Catalytic propensity of biochar decorated with core-shell nZVI@Fe<sub>3</sub>O<sub>4</sub>: A sustainable photo-Fenton catalysis of methylene blue dye and reduction of 4-nitrophenol. *J. Environ. Chem. Eng.* **2022**, *10*, 107401. [\[CrossRef\]](#)
27. Ma, C.; Zhang, Y.; Yin, B.; Chen, J.; Guo, M.; Gao, X. Wood powder biochar in CdS-WPB-g-C<sub>3</sub>N<sub>4</sub> heterojunction as an electron transfer medium for enhancing photocatalytic performance toward degradation methyl orange. *J. Environ. Chem. Eng.* **2023**, *11*, 109135. [\[CrossRef\]](#)
28. Zhu, Y.; Ji, S.; Liang, W.; Li, C.; Nie, Y.; Dong, J.; Shi, W.; Ai, S. A low-cost and eco-friendly powder catalyst: Iron and copper nanoparticles supported on biochar/geopolymer for activating potassium peroxymonosulfate to degrade naphthalene in water and soil. *Chemosphere* **2022**, *303 Pt 2*, 135185. [\[CrossRef\]](#)
29. Alshahrani, H.; Arun Prakash, V.R. Mechanical, fatigue and DMA behaviour of high content cellulosic corn husk fibre and orange peel biochar epoxy biocomposite: A greener material for cleaner production. *J. Clean. Prod.* **2022**, *374*, 133931. [\[CrossRef\]](#)
30. Li, Y.; Zimmerman, A.R.; He, F.; Chen, J.; Han, L.; Chen, H.; Hu, X.; Gao, B. Solvent-free synthesis of magnetic biochar and activated carbon through ball-mill extrusion with Fe<sub>3</sub>O<sub>4</sub> nanoparticles for enhancing adsorption of methylene blue. *Sci. Total Environ.* **2020**, *722*, 137972. [\[CrossRef\]](#)
31. Wang, H.; Duan, R.; Zhou, X.; Wang, J.; Liu, Y.; Xu, R.; Liao, Z. Efficient removal of mercury and chromium from wastewater via biochar fabricated with steel slag: Performance and mechanisms. *Front. Bioeng. Biotechnol.* **2022**, *10*, 961907. [\[CrossRef\]](#)
32. Wei, A.; Ma, J.; Chen, J.; Zhang, Y.; Song, J.; Yu, X. Enhanced nitrate removal and high selectivity towards dinitrogen for groundwater remediation using biochar-supported nano zero-valent iron. *Chem. Eng. J.* **2018**, *353*, 595–605. [\[CrossRef\]](#)
33. Luo, Q.; Chen, D.; Cui, T.; Duan, R.; Wen, Y.; Deng, F.; Li, L.; Wang, H.; Zhang, Y.; Xu, R. Selenite elimination via zero-valent iron modified biochar synthesized from tobacco straw and copper slag: Mechanisms and agro-industrial practicality. *Front. Bioeng. Biotechnol.* **2022**, *10*, 1054801. [\[CrossRef\]](#)
34. Pozo, C.; Rego, F.; Yang, Y.; Puy, N.; Bartrolí, J.; Fàbregas, E.; Bridgwater, A.V. Converting coffee silverskin to value-added products by a slow pyrolysis-based biorefinery process. *Fuel Process Technol.* **2021**, *214*, 106708. [\[CrossRef\]](#)
35. Mahmoud, M.E.; Mohamed, A.K.; Salam, M.A. Self-decoration of N-doped graphene oxide 3-D hydrogel onto magnetic shrimp shell biochar for enhanced removal of hexavalent chromium. *J. Hazard. Mater.* **2021**, *408*, 124951. [\[CrossRef\]](#)
36. Xia, J.; Shen, Y.; Zhang, H.; Hu, X.; Mian, M.M.; Zhang, W.H. Synthesis of magnetic nZVI@biochar catalyst from acid precipitated black liquor and Fenton sludge and its application for Fenton-like removal of rhodamine B dye. *Ind. Crops Prod.* **2022**, *187*, 115449. [\[CrossRef\]](#)
37. Xu, Z.; Xu, X.; Zhang, Y.; Yu, Y.; Cao, X. Pyrolysis-temperature depended electron donating and mediating mechanisms of biochar for Cr(VI) reduction. *J. Hazard. Mater.* **2020**, *388*, 121794. [\[CrossRef\]](#)
38. Kumaraswamy, R.V.; Saharan, V.; Kumari, S.; Choudhary, R.C.; Pal, A.; Sharma, S.S.; Rakshit, S.; Raliya, R.; Biswas, P. Chitosan-silicon nanofertilizer to enhance plant growth and yield in maize (*Zea mays* L.). *Plant Physiol. Biochem* **2021**, *159*, 53–66. [\[CrossRef\]](#)
39. Wang, H.; Wen, Y.; Ding, Y.; Yue, Z.; Xu, D.; Liu, Y.; Zhang, Y.; Xu, R.; Zeng, W. Rapid and Effective Lead Elimination Using Cow Manure Derived Biochar: Balance between Inherent Phosphorus Release and Pollutants Immobilization. *Toxics* **2022**, *11*, 1.
40. Yang, X.; Zhu, W.; Chen, F.; Song, Y.; Yu, Y.; Zhuang, H. Modified biochar prepared from *Retinervus luffae fructus* for dyes adsorption and aerobic sludge granulation. *Chemosphere* **2023**, *322*, 138088. [\[CrossRef\]](#)
41. Wang, H.; Liu, Y.; Ifthikar, J.; Shi, L.; Khan, L.; Chen, Z.; Chen, Z. Towards a better understanding on mercury adsorption by magnetic bio-adsorbents with gamma-Fe<sub>2</sub>O<sub>3</sub> from pinewood sawdust derived hydrochar: Influence of atmosphere in heat treatment. *Bioresour. Technol.* **2018**, *256*, 269–276. [\[CrossRef\]](#) [\[PubMed\]](#)
42. Truong, Q.-M.; Ho, P.-N.; Nguyen, T.-B.; Chen, W.-H.; Bui, X.-T.; Patel, A.K.; Singhania, R.R.; Chen, C.-W.; Dong, C.-D. Magnetic biochar derived from macroalgal *Sargassum hemiphyllum* for highly efficient adsorption of Cu(II): Influencing factors and reusability. *Bioresour. Technol.* **2022**, *361*, 127732. [\[CrossRef\]](#) [\[PubMed\]](#)
43. Yan, N.; Hu, B.; Zheng, Z.; Lu, H.; Chen, J.; Zhang, X.; Jiang, X.; Wu, Y.; Dolfing, J.; Xu, L. Twice-milled magnetic biochar: A recyclable material for efficient removal of methylene blue from wastewater. *Bioresour. Technol.* **2023**, *372*, 128663. [\[CrossRef\]](#) [\[PubMed\]](#)
44. Tian, X.; Yang, R.; Chen, T.; Cao, Y.; Deng, H.; Zhang, M.; Jiang, X. Removal of both anionic and cationic dyes from wastewater using pH-responsive adsorbents of L-lysine molecular-grafted cellulose porous foams. *J. Hazard. Mater.* **2022**, *426*, 128121. [\[CrossRef\]](#)
45. Yu, K.L.; Lee, X.J.; Ong, H.C.; Chen, W.H.; Chang, J.S.; Lin, C.S.; Show, P.L.; Ling, T.C. Adsorptive removal of cationic methylene blue and anionic Congo red dyes using wet-torrefied microalgal biochar: Equilibrium, kinetic and mechanism modeling. *Environ. Pollut.* **2021**, *272*, 115986. [\[CrossRef\]](#)
46. Tran, H.N.; Lima, E.C.; Juang, R.S.; Bollinger, J.C.; Chao, H.P. Thermodynamic parameters of liquid-phase adsorption process calculated from different equilibrium constants related to adsorption isotherms: A comparison study. *J. Environ. Eng.* **2021**, *9*, 106674. [\[CrossRef\]](#)
47. Mechnou, I.; Meskini, S.; El Ayar, D.; Lebrun, L.; Hlaibi, M. Olive mill wastewater from a liquid biological waste to a carbon/oxocalcium composite for selective and efficient removal of methylene blue and paracetamol from aqueous solution. *Bioresour. Technol.* **2022**, *365*, 128162. [\[CrossRef\]](#)

48. Raji, Y.; Nadi, A.; Mechnou, I.; Saadouni, M.; Cherkaoui, O.; Zyade, S. High adsorption capacities of crystal violet dye by low-cost activated carbon prepared from Moroccan Moringa oleifera wastes: Characterization, adsorption and mechanism study. *Diam. Relat. Mater.* **2023**, *135*, 109834. [\[CrossRef\]](#)
49. Mechnou, I.; Meskini, S.; Mourtah, I.; Lebrun, L.; Hlaibi, M. Use of phosphorus-doped microporous carbon from olive mill wastewater for effective removal of Crystal violet and Methylene blue. *J. Clean. Prod.* **2023**, *393*, 136333. [\[CrossRef\]](#)
50. Zhang, Z.; Li, Y.; Zong, Y.; Yu, J.; Ding, H.; Kong, Y.; Ma, J.; Ding, L. Efficient removal of cadmium by salts modified-biochar: Performance assessment, theoretical calculation, and quantitative mechanism analysis. *Bioresour. Technol.* **2022**, *361*, 127717. [\[CrossRef\]](#)
51. Li, H.; Kong, J.; Zhang, H.; Gao, J.; Fang, Y.; Shi, J.; Ge, T.; Fang, T.; Shi, Y.; Zhang, R.; et al. Mechanisms and adsorption capacities of ball milled biomass fly ash/biochar composites for the adsorption of methylene blue dye from aqueous solution. *J. Water Process Eng.* **2023**, *53*, 103713. [\[CrossRef\]](#)
52. Lu, L.; Shan, R.; Shi, Y.; Wang, S.; Yuan, H. A novel TiO<sub>2</sub>/biochar composite catalysts for photocatalytic degradation of methyl orange. *Chemosphere* **2019**, *222*, 391–398. [\[CrossRef\]](#)
53. Liu, J.L.; Qian, W.C.; Guo, J.Z.; Shen, Y.; Li, B. Selective removal of anionic and cationic dyes by magnetic Fe<sub>3</sub>O<sub>4</sub>-loaded amine-modified hydrochar. *Bioresour. Technol.* **2021**, *320 Pt A*, 124374. [\[CrossRef\]](#)
54. Nguyen, X.C.; Nguyen, T.T.H.; Nguyen, T.H.C.; Le, Q.V.; Vo, Y.B.; Tran, T.C.P.; La, D.D.; Kumar, G.; Nguyen, V.K.; Chang, S.; et al. Sustainable carbonaceous biochar adsorbents derived from agro-wastes and invasive plants for cation dye adsorption from water. *Chemosphere* **2021**, *282*, 131009. [\[CrossRef\]](#)
55. Rubangakene, N.O.; Elkady, M.; Elwardany, A.; Fujii, M.; Sekiguchi, H.; Shokry, H. Effective decontamination of methylene blue from aqueous solutions using novel nano-magnetic biochar from green pea peels. *Environ. Res.* **2023**, *220*, 115272. [\[CrossRef\]](#)
56. Eshraghian, A.; Yu, L.; Achari, G.; Sundararaj, U. Development of an effective asphaltene-derived adsorbent for wastewater treatment: Characterization and methyl orange removal study. *J. Environ. Chem. Eng.* **2023**, *11*, 109221. [\[CrossRef\]](#)
57. Sun, Y.; Wang, T.; Han, C.; Lv, X.; Bai, L.; Sun, X.; Zhang, P. Facile synthesis of Fe-modified lignin-based biochar for ultra-fast adsorption of methylene blue: Selective adsorption and mechanism studies. *Bioresour. Technol.* **2022**, *344 Pt A*, 126186. [\[CrossRef\]](#)
58. Zhang, P.; O'connor, D.; Wang, Y.; Jiang, L.; Xia, T.; Wang, L.; Tsang, D.C.; Ok, Y.S.; Hou, D. A green biochar/iron oxide composite for methylene blue removal. *J. Hazard. Mater.* **2020**, *384*, 121286. [\[CrossRef\]](#)
59. Mu, Y.; Du, H.; He, W.; Ma, H. Functionalized mesoporous magnetic biochar for methylene blue removal: Performance assessment and mechanism exploration. *Diam. Relat. Materials* **2022**, *121*, 108795. [\[CrossRef\]](#)
60. Yuan, Y.; Zhang, C.; Zhao, C.; Wang, B.; Wang, X.; Gao, B.; Wang, B.; Rinklebe, J. One-step preparation of a novel graphitic biochar/Cu<sup>0</sup>/Fe<sub>3</sub>O<sub>4</sub> composite using CO<sub>2</sub>-ambiance pyrolysis to activate peroxydisulfate for dye degradation. *J. Environ. Sci.* **2023**, *125*, 26–36. [\[CrossRef\]](#)

**Disclaimer/Publisher's Note:** The statements, opinions and data contained in all publications are solely those of the individual author(s) and contributor(s) and not of MDPI and/or the editor(s). MDPI and/or the editor(s) disclaim responsibility for any injury to people or property resulting from any ideas, methods, instructions or products referred to in the content.